Short Papers

Analysis and Design of Parallel Mechanisms With Flexure Joints

Byoung Hun Kang, John Ting-Yung Wen, Nicholas G. Dagalakis, and Jason J. Gorman

***Abstract*—Flexure joints are frequently used in precision-motion stages and microrobotic mechanisms due to their monolithic construction. The joint compliance, however, can affect the static and dynamic performance of the overall mechanism. In this paper, we consider the analysis and design of general platform-type parallel mechanisms containing flexure joints. Based on static performance measures such as task-space stiffness and manipulability, and constraints such as joint stress, mechanism size, and workspace volume, we pose the design problem as a multiobjective optimization. We first calculate the Pareto frontier, which can then be used to select the desired design parameters based on secondary criteria, such as performance sensitivity and dynamic characteristics. To facilitate design iteration, we apply the pseudo rigid-body approach with a lumped approximation of the flexure joints. A planar mechanism is used to illustrate the analysis and design techniques.**

***Index Terms*—Design optimization, flexure joint, manipulability and stiffness mapping, parallel mechanism, precision stage.**

I. Introduction

Flexure joints offer significant advantages over conventional joints [1], [2] in terms of both ease of manufacturing and operational characteristics. Mechanically assembled joints inevitably reduce accuracy due to manufacturing tolerances. Flexure joints are typically manufactured monolithically, and therefore, avoid assembly errors. The monolithic construction also implies a relatively easy manufacturing process and potentially very compact design. In terms of operation, flexure joints have little friction loss and do not require lubrication. They generate smooth and continuous displacement without backlash. With the suitable choice of material, flexure joints can exhibit a predictable and repeatable relationship between force and displacement. These attributes have endeared flexure mechanisms to meso- and micro-scale precision motion applications, from optical stages to micro-electro-mechanical systems (MEMS). Flexure joints also pose design challenges, however. The behavior of a flexure joint is sensitive to its geometry, therefore, high dimensional accuracy during fabrication is essential and postfabrication calibration is also required. Flexure joints are also susceptible to breakage and fatigue, so they need to be designed to withstand the expected force and displacement in a given application. Flexure joints may also be sensitive to temperature variation as a result of thermal expansion and contraction. This is especially important if thermal actuation is used (e.g., in thermal bimorph). Motion of flexure joints can also be quite complex. For example, a common type of flexure joint, the circular notch hinge, is frequently approximated by a pure rotational joint, but the actual deformation also involves translation.

Thorough treatments of the characterization and design of flexure joints and mechanisms may be found in [1] and [3]. Flexure mechanism design is usually addressed either from a kinematic synthesis point of view with the overall mechanism compliance as a secondary criterion, or from the compliance point of view [1] with the emphasis on synthesizing desired compliance characteristics using, for example, topological optimization [4], [5] or finite-element analysis (FEA) [6], [7].

The goal of this paper is to present new analysis and design tools for parallel mechanisms containing flexure joints. Our approach is to balance the motion and compliance consideration through a multiobjective optimization. To reduce the computation load in the design optimization, we combine the lumped parameter Paros–Weisbord model [8] for the flexure joints and the pseudo rigid-body model for the mechanism. Simulation based on FEA is performed to ensure the validity of this approximation.

In terms of performance, a well-established criterion for serial or parallel mechanisms is the manipulability ellipsoid, which characterizes the task-space motion under normalized active joint motion. This concept was first proposed for serial manipulators [9] and later extended to parallel robots [10], [11]. For general parallel mechanisms, kinematic stability [10], [12] is also important. A mechanism is kinematically stable if it is fully constrained when all the active joints are locked, i.e., there is no uncontrolled motion under external load. For flexure-based parallel mechanisms, the concept of manipulability remains important. However, kinematic stability should be replaced by a stiffness criterion, since the joint stiffness may be used to prevent excessive undesired motion. We therefore pose the design problem as a multiobjective optimization problem, with the performance metrics based on manipulability and stiffness matrices subject to constraints such as the maximum joint stress, workspace, mechanism size, and bounds on the design parameters. The Pareto frontier [13] is then calculated and the final design determined, based on secondary considerations such as dynamic characteristics and performance sensitivity. A 1-D stage designed by the National Institute of Standards and Technology (NIST) is used to illustrate our modeling and design approach.

This paper is organized as follows. The kinematic description of a parallel flexure mechanism is given in Section II. Lumped flexure joint models and their comparison with the FEA results are shown in Section III. The design-optimization approach is presented in Section IV. Application to the NIST stage is shown in Section V.

II. Differential Kinematics

Consider a parallel mechanism with active joints denoted by q_a and passive joints denoted by q_p. The differential kinematics may be described as

$$\begin{bmatrix} \Delta x_T \\ 0 \end{bmatrix} = \underbrace{\begin{bmatrix} J_{T_a} & J_{T_p} \\ J_{C_a} & J_{C_p} \end{bmatrix}}_{J:=\begin{bmatrix} J_T \\ J_C \end{bmatrix}} \underbrace{\begin{bmatrix} \Delta q_a \\ \Delta q_p \end{bmatrix}}_{\Delta q} \tag{1}$$

Manuscript received October 25, 2004. This paper was recommended for publication by Associate Editor J. P. Merlet and Editor F. Park upon evaluation of the reviewers' comments. This work was supported in part by the National Science Foundation under Grant IIS-9820709, and in part by the Center for Automation Technologies under a block grant from the New York State Office of Science, Technology, and Academic Research. This paper was presented in part at the IEEE International Conference on Robotics and Automation, New Orleans, LA, May 2004.

B. H. Kang is with the Department of Mechanical Design Engineering, Korea Polytechnic University, Siheung City, Korea (e-mail: kangb@kpu.ac.kr).

J. T.-Y. Wen is with the Department of Electrical, Computer, and Systems Engineering, Rensselaer Polytechnic Institute, Troy, NY 12180 USA (e-mail: wenj@rpi.edu).

N. G. Dagalakis and J. J. Gorman are with the Intelligent Systems Division, Manufacturing Engineering Laboratory, National Institute of Standards and Technology, Gaithersburg, MD 20899 USA (e-mail: dagalaki@cme.nist.gov; gorman@cme.nist.gov).

Digital Object Identifier 10.1109/TRO.2005.855989

where Δx_T is the incremental task-frame displacement. For parallel mechanisms with conventional passive joints, J_{C_p} is typically square (same number of passive joints as constraints), so that there are no undesirable internal constraint forces. It is also essential to ensure that J_{C_p} is invertible, so that there would not be undesired motion (this is the kinematic stability condition). If J_{C_p} is a tall matrix, the mechanism is overconstrained, and it cannot move unless some of the constraints are redundant. If this is the case for a working mechanism, the rigid-body kinematic description is not adequate, and either more lumped joints need to be added or a distributed description should be used. If J_{C_p} is a fat matrix, the mechanism is underconstrained. For conventional parallel mechanisms, this is not desirable, since there could be uncontrolled motion resulting from external loads. However, we shall see that for flexure mechanisms, this may be acceptable (and, indeed, is usually the case), provided that the stiffness in the direction of unwanted motion is sufficiently large.

We now consider a fully constrained mechanism (when active joints are locked) or underconstrained mechanism, i.e., J_{C_p} is square or fat, and full rank. If J_{C_p} is fat, Δq_p cannot be uniquely solved, since any vector in the null space of J_{C_p} may be added to the solution. In this case, we assume that the solution Δq_p minimizes the strain energy in the passive joints, i.e., Δq_p is found from

$$\min_{\Delta q_p} \frac{1}{2}\Delta q_p^T K_{q_p} \Delta q_p, \quad \text{subject to } 0 = J_{C_a}\Delta q_a + J_{C_p}\Delta q_p \tag{2}$$

where we have assumed linear spring characteristics with spring constant K_{q_p}. We treat Δq_p as the actual joint displacement, since we assume that the joint displacement from the equilibrium is small. The solution of (2) may be readily found

$$\Delta q_p = -J_{C_p}^{\ddagger} J_{C_a} \Delta q_a \tag{3}$$

where $J_{C_p}^{\ddagger}$ is the weighted pseudoinverse of J_{C_p}

$$J_{C_p}^{\ddagger} := K_{q_p}^{-1/2} (J_{C_p} K_{q_p}^{-1/2})^{\dagger} \tag{4}$$

and † denotes the Moore–Penrose pseudoinverse. If J_{C_p} is square invertible, then $J_{C_p}^{\ddagger} = J_{C_p}^{-1}$.

The relationship between active joint displacement and task displacement is then

$$\Delta x_T = \underbrace{(J_{T_a} - J_{T_p} J_{C_p}^{\ddagger} J_{C_a})}_{:= J_{T\text{comp}}} \Delta q_a. \tag{5}$$

By applying the principle of virtual work, we obtain the dual relationship

$$\underbrace{\begin{bmatrix} \tau_a \\ \tau_p \end{bmatrix}}_{\tau} = \begin{bmatrix} J_{T_a}^T & J_{C_a}^T \\ J_{T_p}^T & J_{C_p}^T \end{bmatrix} \begin{bmatrix} f_T \\ f_C \end{bmatrix} \tag{6}$$

where f_T is the externally applied spatial force, f_C is the constraint spatial force [to enforce the kinematic constraint, the bottom portion of (1)], and τ_a and τ_p are the torque vectors applied at the active and passive joints, respectively. When the passive joints are free (e.g., pin, spherical, etc.), $\tau_p = 0$. For flexure joints, we assume that τ_p is related to Δq_p through a linear stiffness (see Section III-A) $\tau_p = K_p \Delta q_p$.

By far the most common configuration of parallel mechanism is a platform supported by multiple legs. For an M-leg platform mechanism, the differential kinematics may be written as

$$\Delta x_T = J_{T\,1}\Delta q_{a\,1} + J_{C\,1}\Delta q_{p\,1} = \ldots = J_{T\,M}\Delta q_{a\,M} + J_{C\,M}\Delta q_{p\,M}. \tag{7}$$

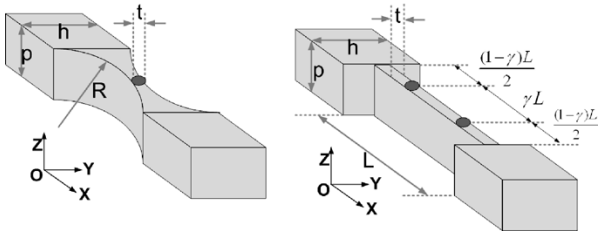

Fig. 1. Flexure joint modeling. (a) Circular notch hinge joint. (b) Cantilevered joint.

We can rewrite this relation as

$$\underbrace{\begin{bmatrix} J_{a\,1} & & & & & \\ & \ddots & & & 0 & \\ & & J_{a\,M} & & & \\ & & & J_{p\,1} & & \\ & 0 & & & \ddots & \\ & & & & & J_{p\,M} \end{bmatrix}}_{J} \begin{bmatrix} \Delta q_{a\,1} \\ \vdots \\ \Delta q_{a\,M} \\ \Delta q_{p\,1} \\ \vdots \\ \Delta q_{p\,M} \end{bmatrix} = \begin{bmatrix} \Delta x_1 \\ \vdots \\ \Delta x_M \end{bmatrix} = \underbrace{\begin{bmatrix} I \\ \vdots \\ I \end{bmatrix}}_{A} \Delta x_T. \tag{8}$$

Since A is of full column rank, we can immediately transform this to the form (1)

$$\Delta x_T = A^{\dagger} J \Delta q \tag{9}$$

$$0 = \widetilde{A} J \Delta q \tag{10}$$

where $A^{\dagger}$ is the pseudoinverse of A, and $\widetilde{A}$ is a full row rank matrix whose null space coincides with the column space of A.

III. Flexure Joint Model

A. Joint Stiffness

We assume a linear spring joint model, i.e., for the ith joint

$$\tau_i = K_{p_i} \Delta q_i. \tag{11}$$

A common type of flexure joint is a circular notch hinge, as shown in Fig. 1(a). Such a joint could have a full 3-D joint stiffness coupling force/torque to translation/rotation [3], [8]. Other similar types of hinge joints with parabolic or hyperbolic shapes may also be considered [14]. Due to the geometry, the inplane rotational and shear stiffness components are dominant. We therefore model it either as a rotational joint [1 degree of freedom (DOF)] or a rotational and shear joint (2 DOF). The stiffness of a pure rotational joint is given by [8]

$$K_r \approx \frac{2Ep}{9\pi} \sqrt{\frac{t^5}{R}} \tag{12}$$

where E is the Young's Modulus of the hinge material, p and t are the thickness and width of the joint, and R is the radius of the circular notch. If the shear translation is also considered, the stiffness is given by [8]

$$K_s \approx \frac{2Ep(2\alpha)^{5/2}}{9\pi(1-\alpha^2)} \tag{13}$$

where $\alpha = t/2R$. The joint location of rotation and shear is assumed to be the same as shown in Fig. 1(a).

A cantilevered flexure may be approximated by two rotational joints, as shown in Fig. 1(b). The joint stiffness for each rotational joint may be approximately modeled as [8]

$$K_c \approx 2\gamma K_\theta \frac{EI}{L} \tag{14}$$

where E is the Young's Modulus, $I = pt^3/12$ is the moment of inertia about the vertical axis, L is the length of the joint, and γ and K_θ are experimentally determined constants

$$\gamma = 0.8517, K_\theta = 2.6762.$$

B. Joint Stress

The stress in a flexure joint is roughly proportional to the deflection of the joint, provided that the deflection is small. For a circular notch joint, it has been shown that the stress σ is related to the angular deflection θ [3]

$$\theta = \frac{3\pi}{4E}\sqrt{\frac{R}{t}}\sigma. \tag{15}$$

For a cantilevered joint, the relationship is approximately

$$\theta = \frac{0.148}{E}\frac{L}{t}\sigma. \tag{16}$$

If the maximum joint stress is given (e.g., from the yield stress of the material), it can be converted to an equivalent maximum joint displacement by using the above formulas.

C. Comparison Between Lumped and FEA Models

The lumped stiffness expression for the flexure joint is only an approximation. To evaluate the quality of this approximation, we compare the stiffness prediction with the FEA result for the following dimension (based on the NIST stage in Section V):

$$t = 0.1 \text{ mm}, R = 0.21 \text{ mm}, p = 6.35 \text{ mm}.$$

The FEA package Ansys 7.0 is used, with 49 000 mesh elements. We assume the flexure is made from 6061-T6 aluminum alloy with Young's Modulus of $E = 70$ GPa.

Using the lumped models (12) and (13), the rotational and shear stiffness coefficients are calculated to be

$$K_r = 0.216 \frac{\text{N-m}}{\text{rad}}, \quad K_s = 5.057 \times 10^6 \frac{\text{N}}{\text{m}}. \tag{17}$$

Either area or line force models may be used in FEA; an area force is exerted on all nodes that are located in a specified area, while a line force is only exerted on the nodes located in a specified direction. With the line force, the stiffness coefficients are

$$K_r = 0.268 \frac{\text{N-m}}{\text{rad}}, \quad K_s = 4.869 \times 10^6 \frac{\text{N}}{\text{m}}. \tag{18}$$

With the area force, the stiffness coefficients are

$$K_r = 0.376 \frac{\text{N-m}}{\text{rad}}, \quad K_s = 4.185 \times 10^6 \frac{\text{N}}{\text{m}}. \tag{19}$$

Comparing these values with the lumped model prediction (17) shows that the line force model gives a better match with the lumped parameter model. This is not too surprising, since the lumped model is derived under the assumption of pure moment and force along the coordinate axes, which is closer to the line force loading condition.

For a circular notch joint, the accuracy of approximation depends on the ratio between the notch radius and joint width, $\beta = R/t$. It has been shown that the quality of the lumped model approximation improves with increasing β [3]. We validated this observation in FEA by comparing the rotational and shear stiffness coefficients for $\beta = 1, 2, \ldots, 10$ (with R fixed at 212.5μm). The results are shown in Figs. 2 and 3 for rotational and shear stiffness, respectively. In both cases, stiffness values from the lumped model and FEA become close for $\beta \geq 2$. As before, the line force model also shows better prediction than the area force model.

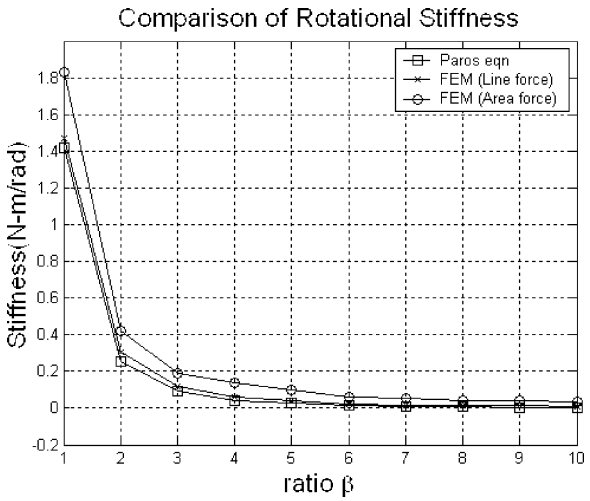

Fig. 2. Rotational stiffness with respect to β.

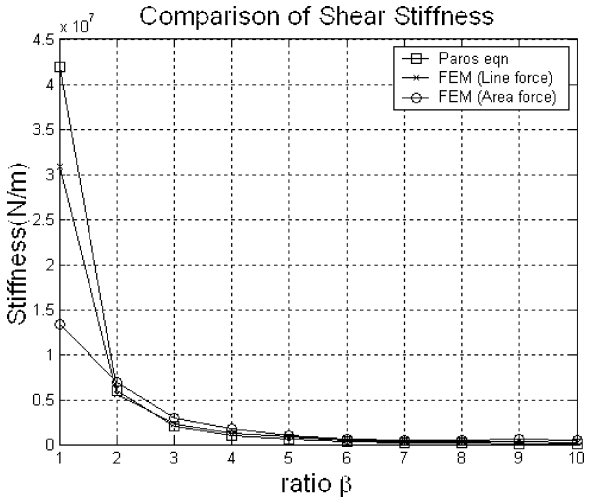

Fig. 3. Shear stiffness with respect to β.

IV. Design Optimization

Design optimization involves selecting a set of design variables w to optimize one or more performance objectives, subject to a set of constraints

$$\min_w \{\mu_1, \mu_2, \ldots\} \text{ subject to } \gamma_i(w) \leq \Gamma_i. \tag{20}$$

A common approach to this multiobjective optimization problem is to first find the Pareto optimal solutions [13], and then use them to guide the selection of the final design choice [15]. A solution is Pareto when a feasible decrease in one design metric causes at least one other design metric to increase. Solutions that are not Pareto are generally discarded, because at least one design metric can be further improved with no cost to any of the other design metrics. The collection of all Pareto

solutions is called the Pareto frontier. To facilitate visualization of design choices, usually only a small number of performance metrics (no more than three) is considered in the optimization, while the rest of the performance metrics are included in the constraints.

For flexure mechanism design, we choose the design variables to be the joint stiffness (which is determined by the joint geometry) and joint locations, the performance metrics based on manipulability and stiffness, and design constraints based on joint stress and mechanism size. Once the Pareto frontier is generated, e.g., by using the normal constraint method [16], secondary criteria such as performance sensitivity, dynamic characteristics, and manufacturability may be used to determine the final design parameters.

A. Manipulability

Manipulability is characterized by $J_{T_{\text{comp}}}$ as in (5). Depending on the design objective, different metrics may be imposed. An important consideration in the choice of design metric is the mixture of different units in $J_{T_{\text{comp}}}$ (due to both translational and rotational components of the task velocity). The danger of ignoring this unit inconsistency has been pointed out in hybrid position/force control [17]. This issue may be addressed by choosing a weighting matrix to balance the translational and rotation components of the motion [18].

If it is desirable to have an isotropic mechanism (the task frame is equally easy to move in all directions, for active joint motion constrained in a unit ball), then the metric to minimize may be

$$\mu_M(J_{T_{\text{comp}}}) = \left(\frac{s_{\max}(J_{T_{\text{comp}}})}{s_{\min}(J_{T_{\text{comp}}})} - 1\right)^2 \tag{21}$$

where $s_{\min}$ and $s_{\max}$ denote the minimum and maximum singular values, respectively (equivalently, the lengths of the principal major and minor axes of the manipulability ellipsoid).

It may also be desirable to maximize the overall workspace. In this case, we can choose to maximize the volume of the manipulability ellipsoid by minimizing the metric

$$\mu_M(J_{T_{\text{comp}}}) = \left(\prod_j s_j(J_{T_{\text{comp}}})\right)^{-1}. \tag{22}$$

If it is desired to increase manipulability in directions given by the unit vectors $\{u_i\}$ and decrease manipulability in directions given by $\{v_i\}$, then a possible metric to minimize is the following weighted sum:

$$\mu_M(J_{T_{\text{comp}}}) = \sum_i \alpha_i \left(u_i^T J_{T_{\text{comp}}}^T J_{T_{\text{comp}}} u_i\right)^{-1} + \sum_i \beta_i \left(v_i^T J_{T_{\text{comp}}}^T J_{T_{\text{comp}}} v_i\right). \tag{23}$$

B. Task-Space Stiffness

The task-space stiffness is defined from the force balance between the applied external spatial force f_T and the corresponding task-frame displacement Δx_T

$$f_T = K_T \Delta x_T. \tag{24}$$

Rewrite the force balance (6) as

$$\tau = J_T^T f_T + J_C^T f_C. \tag{25}$$

By assumption, J_{C_p} is full row rank, therefore, J_C is full row rank. Let $\widetilde{J_C}$ be the full column rank matrix whose column space coincides with the null space of J_C. Then

$$\widetilde{J_C}^T \tau = \widetilde{J_C}^T J_T^T f_T. \tag{26}$$

Substituting in (24) and using the differential kinematics [top portion of (1)], we get

$$\begin{aligned}\widetilde{J_C}^T \tau &= \widetilde{J_C}^T J_T^T K_T \Delta x_T \\ &= \widetilde{J_C}^T J_T^T K_T J_T \Delta q.\end{aligned} \tag{27}$$

Assume the joint torque is related to the joint displacement through a linear spring relationship

$$\begin{bmatrix}\tau_a \\ \tau_p\end{bmatrix} = \underbrace{\begin{bmatrix}K_{q_a} & 0 \\ 0 & K_{q_p}\end{bmatrix}}_{K_q} \begin{bmatrix}\Delta q_a \\ \Delta q_p\end{bmatrix} \tag{28}$$

where K_{q_a} denotes the active joint stiffness, and K_{q_p} denotes the passive joint stiffness. If proportional-derivative type of feedback is used for the active joints, then

$$K_{q_a} = K_{q_a}^{(p)} + K_{q_a}^{(a)} \tag{29}$$

where $K_{q_a}^{(p)}$ denotes the passive portion, and $K_{q_a}^{(a)}$ denotes the proportional feedback gain.

Substituting (28) into (27), we get

$$\widetilde{J_C}^T K_q \Delta q = \widetilde{J_C}^T J_T^T K_T J_T \Delta q. \tag{30}$$

From the kinematic constraint [bottom portion of (1)], we know Δq may be expressed as

$$\Delta q = \widetilde{J_C} \phi \tag{31}$$

for some vector ϕ. Substituting into (30), we get

$$\widetilde{J_C}^T K_q \widetilde{J_C} \phi = \widetilde{J_C}^T J_T^T K_T J_T \widetilde{J_C} \phi. \tag{32}$$

Since this holds for any ϕ, we obtain

$$\widetilde{J_C}^T K_q \widetilde{J_C} = \widetilde{J_C}^T J_T^T K_T J_T \widetilde{J_C} \tag{33}$$

which can be used to solve for the task-space stiffness

$$K_T = (J_T \widetilde{J_C})^{-T} \widetilde{J_C}^T K_q \widetilde{J_C} (J_T \widetilde{J_C})^{-1}. \tag{34}$$

If the mechanism is kinematically stable, i.e., J_{C_p} is square invertible, then

$$\widetilde{J_C} = \begin{bmatrix} I \\ -J_{C_p}^{-1} J_{C_a} \end{bmatrix} \tag{35}$$

and (33) becomes

$$K_{q_a} + J_{C_a}^T J_{C_p}^{-T} K_{q_p} J_{C_p}^{-1} J_{C_a} = J_{T_{\text{comp}}}^T K_T J_{T_{\text{comp}}} \tag{36}$$

which is the same expression as obtained in [19].

Similar to the manipulability matrix, different metrics based on K_T may be used, depending on the application. For example, in [19], the goal is to ensure the stiffness matrix is decoupled. In that case, the metric may be chosen to be

$$\mu_K(K_T) = \left\| K_T \operatorname{diag}(K_T)^{-1} - I \right\| \tag{37}$$

where $\operatorname{diag}(K_T)$ is K_T with all off-diagonal terms set to zeros. If maximum stiffness is desired, the metric may involve maximizing the volume of K_T or minimizing its reciprocal

$$\mu_K(K_T) = \left(\prod_j s_j(K_T)\right)^{-1}. \tag{38}$$

If it is desired to increase stiffness in directions given by the unit vectors $\{u_i\}$ and decrease stiffness in directions given by $\{v_i\}$, a possible metric to minimize is the following weighted sum:

$$\mu_K(J_{T_{\text{comp}}}) = \sum_i \alpha_i \left(u_i^T K_T u_i\right)^{-1} + \sum_i \beta_i \left(v_i^T K_T v_i\right). \tag{39}$$

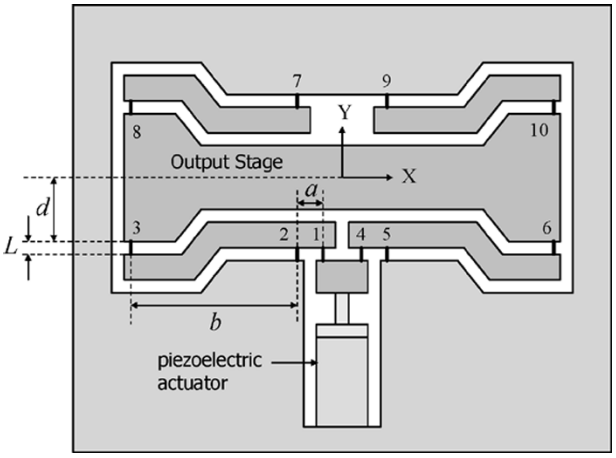

Fig. 4. Schematic of NIST 1-D mechanism.

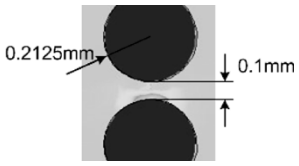

Fig. 5. Flexure joint in NIST 1-D mechanism.

V. Example: NIST 1-D Stage

A. Mechanism Architecture

A 2-DOF macroscale precision motion stage using flexure joints was designed and fabricated by NIST [20], [21]. Several 1-DOF mesoscale (about the size of a credit card) models have also been built [22]. A schematic of the mesoscale mechanism is shown in Fig. 4. A piezoelectric actuator transmits the y-axis motion through joints 1 and 4 to the two lower arms. These arms pivot about joints 2 and 5, and move the output stage through joints 3 and 6. To support the output stage (and to reduce the angular crosstalk, i.e., undesirable angular motion), two additional arms also support the platform through joints 7–10. The goal of the design is to achieve desired manipulability (pure translation in y) and stiffness (large stiffness in the angular and x directions). The joints are constructed as circular notch joints (see Fig. 5 from [20]). However, depending on the exact joint model used, the design result would be different. This is discussed in the next section. By replicating the design along the orthogonal axis, a 2-DOF version has also been designed and built. Such stages are currently being considered for satellite optical communication [23].

B. Kinematic Models

The mechanism consists of six kinematic chains (1–3, 2–3, 4–6, 5–6, 7–8, 9–10) constrained at the platform. This means that there are 15 total constraints [five loops involving (x, y, θ)].

If all the joints in Fig. 4 are chosen to be idealized 1-DOF rotational joints, then there are 10 passive DOFs and the mechanism is overconstrained (J_{C_p} is 15×10). Indeed, in this case, the mechanism cannot move from the equilibrium position shown. This means that the 1-DOF joint approximation is not adequate to describe this mechanism. We consider several possible modifications below; FEA simulation will be used to determine which model gives the closest prediction.

- **Case A**: Replace joints 1, 3, 4, 6, 8, and 10 by two rotational joints connected by a short rigid segment (cantilevered joint model K_c). The motivation of this assumption is to allow rotation, as well as shear type of translation, at these joints. Joints 2, 5, 7, and 9 serve as pivots, and are retained as pure rotational joints (circular notch joint model K_r). In this case, there are 16 passive joints and 15 constraints, i.e., $\widetilde{J_C}$ is rank 2 (including one active joint). Since $J_T \widetilde{J_C}$ [in (33)] is rank 2, only the x-y components of K_T can be determined.
- **Case B**: Replace all joints by double joints (cantilevered joint model K_c). Now there are 20 passive joints and 15 constraints, and K_T may be fully determined.
- **Case C**: Replace all joints by the 2-DOF (rotation + shear) circular notch joint with

$$K_p = \begin{bmatrix} K_r & 0 \\ 0 & K_s \end{bmatrix}.$$

In this case, there are 20 passive joints and 15 constraints, and K_T may also be fully determined.

TABLE I
Overall Stiffness for Cases A, B, C

		w/ K_a (N/m)	w/o K_a (N/m)
Case A	K_x	2.43×10^7	2.43×10^7
	K_y	2.44×10^5	2.86×10^4
Case B	K_x	1.42×10^7	1.42×10^7
	K_y	2.36×10^5	2.02×10^4
Case C	K_x	1.18×10^7	1.18×10^7
	K_y	2.35×10^5	1.91×10^4

w/ K_a: with actuator stiffness, w/o K_a: without actuator stiffness

The flexure mechanism is made from 6061-T6 aluminum alloy. The Young's Modulus is $E = 70$ GPa. The four quadrants of the stage are nominally all symmetric. We use the following dimension:

$$a = 1.5 \text{ mm}, b = 15 \text{ mm}, R = 0.21 \text{ mm}, d = 8.63 \text{ mm}.$$

For cantilevered joints, the passive joint stiffness is calculated using (14) with $L = 2R = 0.42$ mm, $t = 0.1$ mm, and $p = 6.35$ mm

$$K_c = 0.40 \ \frac{\text{N-m}}{\text{rad}}.$$

The actuator stiffness is given by [22]

$$K_a = 2.16 \times 10^7 \ \frac{\text{N}}{\text{m}}.$$

In all cases, the task-space Jacobian is [the task coordinate is arranged as (θ, x, y)]

$$J_{T_{\text{comp}}} = \begin{bmatrix} 0 \\ 0 \\ -10.00 \end{bmatrix}$$

showing only the y-direction motion of the task frame.

The x-y portion of K_T is computed using (33). The result for the three joint assumptions are summarized in Table I. Since the actuator can only move in the y direction, its stiffness K_a only affects the y component of K_T. The x direction stiffness is much lower for **Cases B** and **C** than **Case A**. This is due to the additional DOFs in the joints. To determine which joint model to use, we apply FEA to the mechanism to determine the task-space stiffness as

$$K_x = 1.78 \times 10^7 \ \frac{\text{N}}{\text{m}}, K_y = 1.71 \times 10^4 \ \frac{\text{N}}{\text{m}}.$$

Assuming FEA is a better approximation of the reality than the lumped model, **Cases B** and **C** show better match than **Case A**, indicating the importance of including an additional DOF in the joints. Significant amount of error still remains, but we shall see that the trend (in stiffness) remains valid for the model to be used for design optimization.

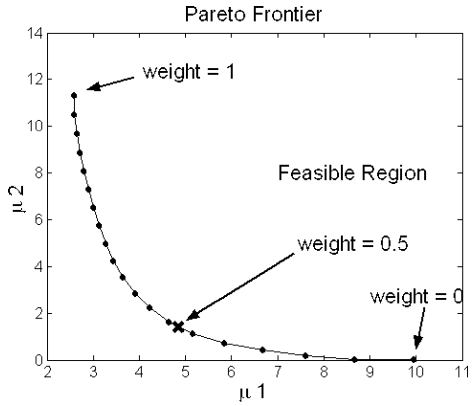

Fig. 6. Pareto frontier for joint model C.

C. Design Optimization

To illustrate the design-optimization procedure, we choose to maximize the y-direction manipulability and the relative stiffness between the x and y directions. The following performance measures are selected:

$$\mu_1 = \frac{10^2}{\left\| J^{(y)}_{T_{\text{comp}}} \right\|} \tag{40}$$

$$\mu_2 = \frac{10^3}{\frac{K_x}{K_y}}. \tag{41}$$

Note that scaling constants are added to normalize between the two measures.

For the maximum joint stress constraint, we use the yield stress for AL6061-T6, $\sigma_{\max} = 220$ MPa. The maximum stress constraint is imposed when the active joint is at its maximum extension $\Delta q_{a_{\max}} = 9.1$ μm. Equations (15) and (16) are used to calculate the joint stress for circular notch joints and cantilevered joints, respectively. In this case, the maximum allowed joint deflection for the circular notch joint is 0.62°, and for the cantilevered joint 0.11°. The design parameters are chosen to be (a, b, L, t) with the bounds (based on maximum overall size and manufacturability)

$$\begin{aligned} 0.5 \text{ mm} \le a \le 4.5 \text{ mm} \\ 5 \text{ mm} \le b \le 45 \text{ mm} \\ 0.142 \text{ mm} \le L \le 1.275 \text{ mm} \\ 0.03 \text{ mm} \le t \le 0.3 \text{ mm}. \end{aligned}$$

Since the stiffness of joint models B and C match similarly with the FEA prediction, and both are better than the joint model A, we will only consider joint model C.

The Pareto frontier for joint model C is calculated using the normal constraint method [16] in MATLAB, and is shown in Fig. 6, which contains all the Pareto solutions. Additional considerations, such as parameter sensitivity or dynamics characteristics, are usually used to determine the final design. As an example, we combine the two design metrics with equal weights

$$\mu = 0.5\mu_1 + 0.5\mu_2.$$

The resulting design variables are shown in Table II. The corresponding manipulability and stiffness are

$$\begin{aligned} J_y = 20.61 \frac{\text{N}}{\text{m}},\ K_x = 4.11 \times 10^7 \frac{\text{N}}{\text{m}} \\ K_y = 0.71 \times 10^4 \frac{\text{N}}{\text{m}}\ \frac{K_y}{K_x} = 0.17 \times 10^{-3}. \end{aligned}$$

TABLE II
INITIAL VERSUS FINAL DESIGN VARIABLES

	Initial Values	Final Design
a	1.5 mm	0.92 mm
b	15 mm	18.9 mm
L	0.425 mm	0.179 mm
t	0.1 mm	0.067 mm

Compared with the nominal design (from Table I, without K_a)

$$\begin{aligned} J_y = 10, K_x = 1.18 \times 10^7 \frac{\text{N}}{\text{m}}, K_y = 1.91 \times 10^4 \frac{\text{N}}{\text{m}} \\ \frac{K_y}{K_x} = 1.62 \times 10^{-3} \end{aligned}$$

it is clear that both μ_1 and μ_2 are improved. To validate this design, FEA simulation is performed with the final design variables, with the following manipulability and stiffness values:

$$\begin{aligned} J_y = 19.10, K_x = 3.7 \times 10^7 \frac{\text{N}}{\text{m}}, K_y = 1.14 \times 10^4 \frac{\text{N}}{\text{m}} \\ \frac{K_y}{K_x} = 3.08 \times 10^{-4}. \end{aligned}$$

Though these values (especially stiffness) deviate from those predicted by the pseudo rigid-body model, both μ_1 and μ_2 still improve over the nominal design.

VI. CONCLUSION

In this paper, we have presented new analysis and design tools for parallel flexure mechanisms. The key difference between flexure mechanisms and parallel mechanisms with conventional joints is that kinematic stability is no longer a design consideration. Instead, task-space stiffness needs to be designed to avoid undesired motion in the presence of external loads. We pose the design problem as a multiobjective optimization, with manipulability and stiffness as performance measures, and maximum joint stress and design parameter bounds as constraints. A 1-D stage designed by NIST is used as an example to illustrate the modeling and design approach. It is shown that a design with equal weighting on manipulability and relative stiffness improves over the nominal design. We also note that the different joint assumptions can significantly affect the result. By using FEA as a validation tool, we show that a 2-DOF circular notch joint (with rotation and shear) performs better than other lumped joint models. We are currently incorporating out-of-plane stiffness in the performance criterion, as well as pursuing designs for different micromechanisms, including microgrippers and multi-DOF planar stages.

REFERENCES

[1] L. L. Howell, *Compliant Mechanisms*. New York: Wiley, 2001.
[2] S. Kota, "Compliant systems using monolithic mechanisms," *Smart Mater. Bull.*, pp. 7–9, Mar. 2000.
[3] S. T. Smith, *Flexures: Elements of Elastic Mechanisms*. New York: Gordon and Breach, 2000.
[4] S. Kota, J. Joo, Z. Li, S. M. Rodgers, and J. Sniegowski, "Design of compliant mechanisms: Applications to MEMS," *Analog Integr. Circuits Signal Process.*, vol. 29, pp. 7–15, 2001.
[5] G. K. Ananthasuresh and M. Frecker, "Synthesis of compliant mechanisms using continuum models," in *Compliant Mechanisms*, L. Howell, Ed. New York: Wiley, 2001.
[6] M. L. Culpepper and G. Anderson, "Design of a low-cost nano-manipulator which utilizes a monolithic, spatial compliant mechanism," *J. Precision Eng.*, vol. 28, pp. 469–482, 2004.
[7] H. H. Pham and I.-M. Chen, "Optimal synthesis for workspace and manipulability of parallel flexure mechanism," in *Proc. 11th World Congr. Mech. Mach. Sci.*, Tianjin, China, 2003, [CD-ROM].

[8] J. M. Paros and L. Weisbord, "How to design flexure hinges," *Mach. Des.*, pp. 151–156, 1965.
[9] T. Yoshikawa, "Manipulability of robotic mechanisms," *Int. J. Robot. Res.*, vol. 4, no. 2, pp. 3–9, 1985.
[10] J. T. Wen and L. S. Wilfinger, "Kinematic manipulability of general constrained rigid multibody systems," *IEEE Trans. Robot. Autom.*, vol. 15, no. 3, pp. 558–567, Jun. 1999.
[11] A. Bicchi and D. Prattichizzo, "Manipulability of cooperation robots with passive joints," in *Proc. IEEE Int. Conf. Robot. Autom.*, 1998, pp. 1038–1044.
[12] F. Park and J. Kim, "Manipulability and singularity analysis of multiple robotic systems: A geometric approach," in *Proc. Int. Conf. Robot. Autom.*, Leuven, Belgium, May 1998, pp. 1032–1037.
[13] A. Ismail-Yahaya and A. Messac, "Required relationship between objective function and Pareto frontier orders: Practical implications," *Am. Inst. Aeronaut. Astronaut. J.*, vol. 39, no. 11, pp. 2168–2174, 2001.
[14] N. Lobontiu, J. S. N. Paine, E. O'Malley, and M. Samuelson, "Parabolic and hyperbolic flexure hinges, motion precision and stress characterization based on compliance closed-form equations," *J. Precision Eng.*, vol. 26, pp. 183–192, 2002.
[15] A. Messac, S. Gupta, and B. Akbulut, "Linear physical programming: A new approach to multiobjective optimization," *Trans. Oper. Res.*, vol. 8, pp. 39–59, Oct. 1996.
[16] A. Ismail-Yahaya and A. Messac, "Effective generation of the Pareto frontier using the normal constraint method," in *Proc. 40th Aerosp. Sci. Meet. Exhib.*, Reno, NV, Jan. 2002, [CD-ROM].
[17] J. Duffy, "The fallacy of modern hybrid control theory that is based on orthogonal complements of twist and wrench spaces," *J. Robot. Syst.*, vol. 7, no. 2, pp. 139–144, Feb. 1990.
[18] J. T. Wen and S. H. Murphy, "Position and force control of robot arms," *IEEE Trans. Autom. Control*, vol. 36, no. 3, pp. 365–374, Mar. 1991.
[19] G. Alici and B. Shirinzadeh, "Kinematics and stiffness analyses of a flexure-jointed planar micromanipulation system for a decoupled compliant motion," in *Proc. IEEE/RSJ Int. Conf. Intell. Robots Syst.*, Las Vegas, NV, Oct. 2003, pp. 3282–3287.
[20] E. Amatucci, N. G. Dagalakis, J. A. Kramar, and F. E. Scire, "Performance evaluation of a parallel cantilever biaxial micropositioning stage," in *Proc. Am. Soc. Precision Eng., 15th Annu. Meet.*, Scottsdale, AZ, 2000, [CD-ROM].
[21] N. G. Dagalakis, J. A. Kramar, E. Amatucci, and R. Bunch, "Kinematic modeling and analysis of a planar micropositioner," in *Proc. Am. Soc. Precision Eng., 16th Annu. Meet.*, Crystal City, VA, 2001, pp. 135–138.
[22] J. J. Gorman, N. G. Dagalakis, and B. G. Boone, "Multi-loop control of a nanopositioning mechanism for ultra-precision beam steering," in *Proc. SPIE Conf. Free-Space Laser Commun. Active Laser Illumin. III*, vol. 5160, San Diego, CA, 2003, pp. 170–181.
[23] B. G. Boone, R. S. Bokulic, G. B. Andrewsa, R. L. McNutt, Jr., and N. Dagalakis, "Optical and microwave communications system conceptual design for a realistic interstellar explorer," in *Proc. SPIE Conf. Free-Space Laser Commun. Active Laser Illumin. II*, vol. 4821, Seattle, WA, Jul. 2002, pp. 225–236.

Vibration-Based Terrain Classification for Planetary Exploration Rovers

Christopher A. Brooks and Karl Iagnemma

***Abstract*—Safe, autonomous mobility in rough terrain is an important requirement for planetary exploration rovers. Knowledge of local terrain properties is critical to ensure a rover's safety on slopes and uneven surfaces. Visual features are often used to classify terrain; however, vision can be sensitive to lighting variations and other effects. This paper presents a method to classify terrain based on vibrations induced in the rover structure by wheel–terrain interaction during driving. This sensing mode is robust to lighting variations. Vibrations are measured using an accelerometer mounted on the rover structure. The classifier is trained using labeled vibration data during an offline learning phase. Linear discriminant analysis is used for online identification of terrain classes, such as sand, gravel, or clay. This approach has been experimentally validated on a laboratory testbed and on a four-wheeled rover in outdoor conditions.**

***Index Terms*—Mobile robots, pattern classification, robot sensing systems, rough terrain.**

I. Introduction

Planetary exploration rovers are being proposed for missions to increasingly challenging locations [1]. These may include craters, hills, and ravines, where rocky outcrops might yield glimpses of a planet's history. To safely traverse slopes and highly uneven terrain, knowledge of local terrain properties is critical, since terrain conditions can strongly influence rover mobility. For example, a rover might climb a rocky slope with ease, but slide down a sandy slope of the same grade. Similarly, a rover traversing loose sand could become entrenched, where a rover crossing packed soil would face no such danger. Terrain-class knowledge would allow a rover to adapt its control and/or planning strategy to safely and efficiently traverse terrain of varying compositions.

Previous research on terrain classification has focused mainly on remote classification using vision or range data. Navigation systems employing these data have been demonstrated by researchers at the Jet Propulsion Laboratory, the National Institute of Standards and Technology, and Carnegie Mellon University [2]–[4]. Classification algorithms that rely on visual features (such as color or texture) are often sensitive to variations in illumination. In addition, vision-based classifiers usually detect features associated with the topmost terrain surface, which may not be the load-bearing surface of interest. An example of this is vegetation-covered terrain, or crusty Mars terrain covered by a thin layer of drift material. Recently, researchers have developed methods for estimating the location of this load-bearing surface [5]. Note, however, that this is not a classification method.

Other algorithms have employed range data to emphasize detection of geometric obstacles, such as rocks or steep slopes [6], [7]. These papers do not explicitly classify terrain, or address the issue of the soil itself being a hazard. Such a hazard can be termed a *nongeometric*

Manuscript received February 28, 2005. This paper was recommended for publication by Associate Editor P. Dupont and Editor S. Hutchinson upon evaluation of the reviewers' comments. This work was supported by the NASA Jet Propulsion Laboratory under the Mars Technology Program. This paper was presented in part at the IEEE International Conference on Robotics and Automation, Barcelona, Spain, April 2005.

The authors are with the Department of Mechanical Engineering, Massachusetts Institute of Technology, Cambridge, MA 02139 USA (e-mail: cabrooks@mit.edu; kdi@mit.edu).

Digital Object Identifier 10.1109/TRO.2005.855994